

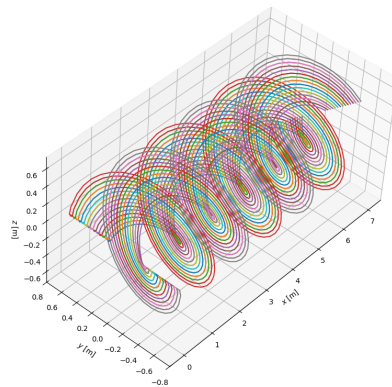
# Lifting Line Model on a Propeller

## AE4135 ROTOR / WAKE AERODYNAMICS

by

### Group 21

Chirag Bansal (6137776)  
Ninad Gajanan (6272053)  
Tanmay Gupta (6170455)



Instructor: Dr. Wei Yu  
Faculty: Faculty of Aerospace Engineering, Delft  
Date: June 5, 2025

# Contents

<b>1</b>	<b>Introduction</b>	<b>1</b>
1.1	The Lifting Line Theory . . . . .	1
1.2	Case Setup: Propeller Analysis . . . . .	1
<b>2</b>	<b>Flowchart</b>	<b>2</b>
<b>3</b>	<b>Assumptions</b>	<b>3</b>
<b>4</b>	<b>Results</b>	<b>4</b>
4.1	Non-dimensional parameters used . . . . .	4
4.2	Comparative study of LLM and BEM . . . . .	4
4.2.1	Radial Distribution of the $\phi$ . . . . .	4
4.2.2	Radial Distribution of the $\alpha$ . . . . .	5
4.2.3	Radial Distribution of $\Gamma$ . . . . .	6
4.2.4	Radial Distribution of the Tangential Load . . . . .	6
4.2.5	Radial Distribution of the Axial Load . . . . .	7
4.2.6	Radial Distribution of the Induction Factor . . . . .	8
4.2.7	Thrust ( $C_T$ ) and Power Coefficient ( $C_P$ ) . . . . .	9
4.3	Sensitivity Analysis . . . . .	9
4.3.1	Assumed Convection Speed for Frozen Wake . . . . .	9
4.3.2	Type of blade segmentation . . . . .	11
4.3.3	Number of Vortex Filaments . . . . .	12
4.3.4	Wake Length . . . . .	14
<b>5</b>	<b>Conclusion</b>	<b>15</b>
<b>6</b>	<b>References</b>	<b>16</b>

## List of Figures

1	Propeller blade force decomposition. . . . .	1
2	Flowchart for Lifting Line solver. . . . .	2
3	Radial distribution of $\phi$ . . . . .	4
4	Radial distribution of $\alpha$ . . . . .	5
5	Radial distribution of $\Gamma$ . . . . .	6
6	Radial distribution of tangential load. . . . .	7
7	Radial distribution of axial load. . . . .	7
8	Radial distribution of axial induction, $a$ . . . . .	8
9	Radial distribution of tangential induction, $a$ . . . . .	8
10	Sensitivity of $\alpha$ and $\phi$ to change in wake velocity. . . . .	9
11	Sensitivity comparison of axial and tangential load for assumed convection speed. . . . .	10
12	Sensitivity comparison of radial distribution of $\Gamma$ . . . . .	10
13	Sensitivity Results of discretisation of blade on $\alpha$ and $\phi$ . . . . .	11
14	Sensitivity comparison of axial and tangential loads for discretisation of blade . . . . .	11
15	Sensitivity results comparison of $\Gamma$ for discretisation of blade . . . . .	11
16	Sensitivity Results of no. of wake segments of $\alpha$ and $\phi$ . . . . .	12
17	Sensitivity comparison of axial and tangential loads for number of wake segments . . . . .	13
18	Sensitivity results comparison of $\Gamma$ for number of wake segments . . . . .	13

19	Sensitivity Results of wake length of $\alpha$ and $\phi$ . . . . .	14
20	Sensitivity comparison of axial and tangential loads for wake length . . . . .	14
21	Sensitivity of $\Gamma$ to wake length . . . . .	14
22	LLM sensitivity to wake length . . . . .	14

**List of Tables**

1	Comparison of BEM and LLM results at different advance ratios . . . . .	9
---	---	---

# 1 Introduction

## 1.1 The Lifting Line Theory

The Lifting Line Model is a simplified aerodynamic model based on the potential flow theory. It is used to analyze the lift distribution and drag characteristics of finite wings, however, it can be applied to rotors as well. It approximates the 3D flow around a lifting surface by considering the rotor blade as a single line— the lifting line, typically located at quarter chord of the blade, where all the bound circulations are concentrated. From every point of this line, a trailing vortex is shed downstream into the wake which follows the local flow.

$$L' = \rho_{\infty} V_{local} \Gamma \quad (1)$$

The core principle of the model is the Kutta-Joukowski theorem which related the lift on a section to its local circulation and velocity using [Equation 1](#). However, the complexity arises due to the velocities induced by the vortex system that alters the effective angle of attack experienced by each blade segment. Due to this effective change in angle of attack, the lift and drag characteristics vary.

An iterative procedure is employed to solve for the lifting line problem. Following an initial guess for the circulation,  $\Gamma$ , typically unit magnitude, the induced velocities are calculated,  $[u', v', w']$ , at various control points using the Biot-Savart law (see [Equation 8](#)) for all vortex elements. A more detailed explanation how the lifting line model is implemented can be seen in [section 2](#). This theory provides a mathematical framework to determine the spanwise load distribution.

## 1.2 Case Setup: Propeller Analysis

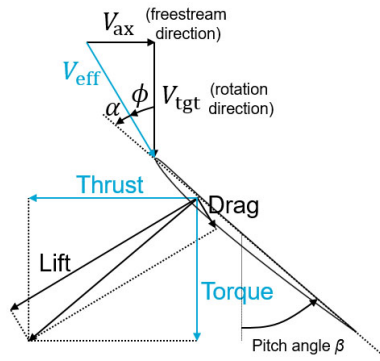


Figure 1: Propeller blade force decomposition.

This assignment focuses on implementing a lifting line model to analyze a propeller operating in cruise. The propeller geometry is given as— radius,  $R = 0.70$  m, number of blades = 6, and features the ARA-D8% airfoil. Performance will be evaluated at Advance ratios of  $J \in \{1.6, 2.0, 2.4\}$ . The propeller operates at  $V_{\infty} = 60$  m/s, and an altitude of  $h = 2000$  m under standard atmospheric conditions.

Using the lifting line framework, key performance parameters such as thrust, torque, power are calculated. Additionally, sensitivity of the results to change in different parameters is studied in [subsection 4.3](#). This analysis will provide insights into the effectiveness of the lifting line theory for modeling propeller aerodynamics. Further, the comparison of the lifting line model to the blade element momentum theory model is analyzed, to assess the accuracy of the model.

## 2 Flowchart

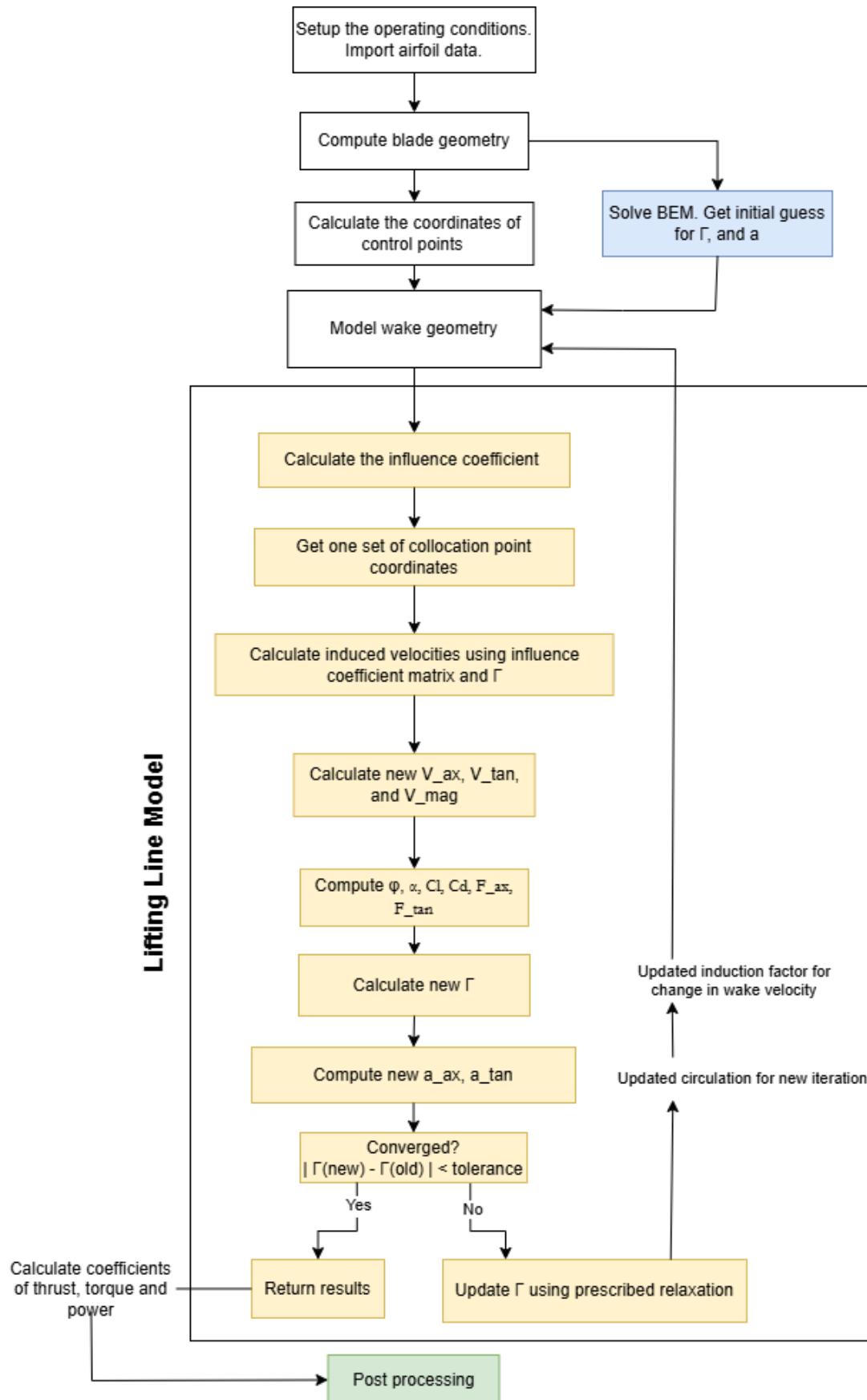


Figure 2: Flowchart for Lifting Line solver.

### 3 Assumptions

The Lifting Line model is based on the potential flow theory and works on certain assumptions. These assumptions are given below.

- The model uses the thin airfoil theory and assumes the flow angle of attack is small. This implies that the wake is aligned with the local velocity
- The flow around the rotor is inviscid, incompressible and irrotational, which allows for the potential flow theory to be used.
- The rotor is modeled by a lifting line, which is a bound vortex at the quarter chord location of the blade
- As the flow convects, the vortices are shed in the form of the trailing vortices from each blade segment.
- Conditions of the Helmholtz's theorems are followed, which are:
  - The strength of the vortex line is constant along its length
  - A vortex line cannot end in the fluid, it must extend to the boundaries of the fluid (i.e. until infinity) or form a closed path
  - A fluid element that is initially irrotational remains irrotational
- Wake is fixed (or frozen), implying that the wake does not deform under the influence of induced velocities
- The flow is steady, time derivatives in the conservation equations can be neglected. In reality, there are unsteady effect due to turbulence which lifting line model does not account
- Rotor blade is discretised into small segments and thus 2D airfoil properties can be used

## 4 Results

The lifting line model is used to solve various flow conditions as given in [subsection 1.2](#). The important non-dimensional parameters have been tabulated, and the results of the radial distribution of angle of attack ( $\alpha$ ), inflow angle ( $\phi$ ), circulation ( $\Gamma$ ), azimuthal ( $F_{tan}$ ) and axial ( $F_{ax}$ ) loads, and the azimuthal( $a'$ ) and axial ( $a$ ) induction factors have been plotted and discussed. A sensitivity analysis is also conducted by varying the initial induction factor, type of blade discretisation, wake length, and number of vortex filaments.

### 4.1 Non-dimensional parameters used

Propeller thrust, and power are non-dimensionalised for scalability and easy comparability of results, and study the performance characteristics. The non-dimensionalisation of all necessary factors is performed as given below.

- Thrust and power coefficient: The coefficients are normalized with the density( $\rho$ ), rotational speed (rps:  $n$ ), and the blade diameter( $D$ )

$$C_T = \frac{T}{\rho n^2 D^4}, \quad C_P = \frac{P}{\rho n^3 D^5} \quad (2)$$

- Normalized Radius: The local radius of the segments or control points have been normalized with the radius of the blade.

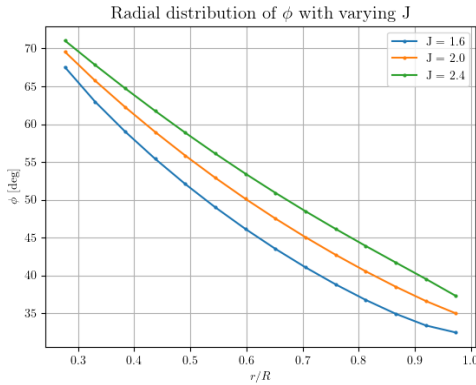
$$\text{Normalized radius} = \frac{r}{R} \quad (3)$$

- Advance ratio: The advance ratio( $J$ ) is defined as the ratio of the speed of the vehicle, or in this case, the freestream velocity, and the rotational speed of the propeller.

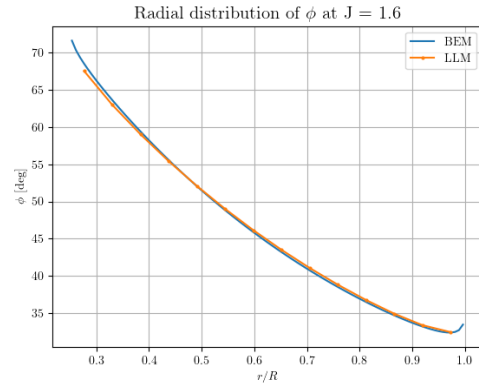
$$J = \frac{V_\infty}{nD} \quad (4)$$

### 4.2 Comparative study of LLM and BEM

#### 4.2.1 Radial Distribution of the $\phi$



(a)  $\phi$  at varying  $J$



(b)  $\phi$  distribution from LLM and BEM

Figure 3: Radial distribution of  $\phi$ .

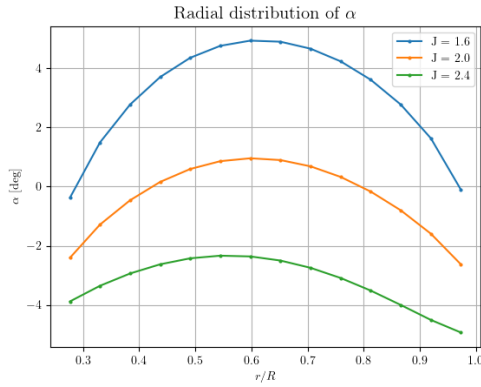
As seen in Figure 3, the inflow angle ( $\phi$ ) decreases progressively from root to tip across all advance ratios. This aligns since as one moves from root to tip, the contribution of the tangential velocity component increases, reducing the inflow angle given by Equation 5. The inflow angle increases with increase in advance ratio (see Figure 3a) as the advance ratio is dictated by the freestream velocity (kept constant) and the blade RPS, (see Equation 4). Increasing blade RPS increases the inflow angle (Equation 5).

$$\phi = \tan^{-1} \left( \frac{V_{ax}}{V_{tan}} \right) = \tan^{-1} \left( \frac{V_{\infty}(1+a)}{\Omega r(1-a')} \right) \quad (5)$$

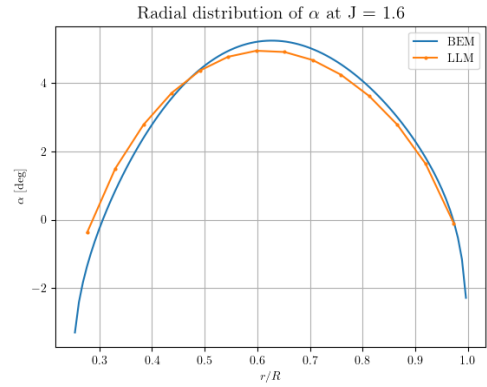
In (Equation 5),  $a$  and  $a'$  are the axial and tangential induction factors respectively,  $\Omega$  is the angular velocity, and  $r$  is the local radius.

Figure 3b shows the comparison of inflow angle between BEM and LLM for  $J = 1.6$ . Both methods show nearly identical trends, indicating strong agreement. Minor deviations occur near the blade ends this is due to the Prandtl corrections imperative to BEM, however, the alignment confirms that both methods consistently capture the local flow angle variation along the span.

#### 4.2.2 Radial Distribution of the $\alpha$



(a)  $\alpha$  at varying  $J$



(b)  $\alpha$  distribution from LLM and BEM

Figure 4: Radial distribution of  $\alpha$ .

As seen in Figure 4, the radial distribution of angle of attack ( $\alpha$ ) shows clear variation across the blade span and with changing advance ratio. The general trend of the  $\alpha$  variation is due to the geometry of the blade. The angle of attack is given by

$$\alpha = \beta - \phi \quad (6)$$

where  $\beta$  is the blade twist. In Figure 4a, it is observed that for lower advance ratios (e.g.,  $J = 1.6$ ), the angle of attack is higher across the span. As  $J$  increases, the overall  $\alpha$  distribution shifts downward. due to increase in the inflow angle. The peak  $\alpha$  consistently occurs at mid-span,  $r/R \in [0.6, 0.7]$ .

Figure 4b shows the comparison between LLM and BEM theory at  $J = 1.6$ . The results show close agreement throughout most of the blade span, with minor deviations, especially near the root. These differences can be attributed to assumptions of both the models, the vortex-induced velocities, and the wake modeling accuracy in the LLM, and the Prandtl corrections in BEM. LLM, however, gives a more physically accurate  $\alpha$  distribution since it explicitly considers the trailing vortices instead of relying on analytically modelled loss factors as in BEM.



### 4.2.3 Radial Distribution of $\Gamma$

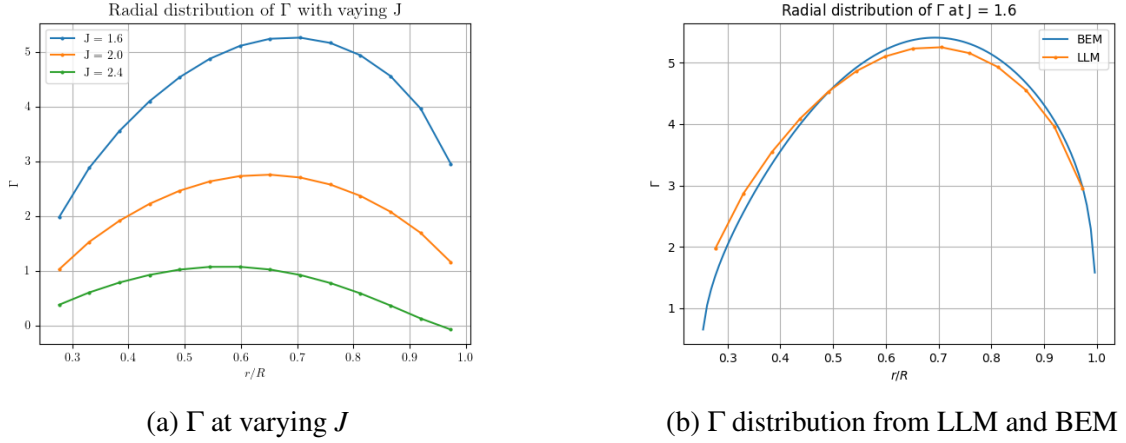


Figure 5: Radial distribution of  $\Gamma$

From Figure 5a, it is evident that circulation decreases with increasing advance ratio. At lower  $J$ , due to higher angle of attack (and inherently higher sectional lift,  $L'$ ), circulation strength increases (see Equation 7).

$$L' = \rho V_{loc} \Gamma \quad (7)$$

LLM predicts a similar trend in the circulation as the BEM model, with a slight offset in the mid-span region. This shows that the formulation of the horseshoe vortex system is accurate, and using the Biot-Savart law, correct values of induced velocities, and hence circulation, are obtained. The induced velocity  $\vec{u}_\omega$  at a control point due to a vortex segment is given by:

$$\vec{u}_\omega = \frac{\Gamma}{4\pi} \int_a^b \frac{d\vec{l} \times \vec{r}}{|\vec{r}|^3} \quad (8)$$

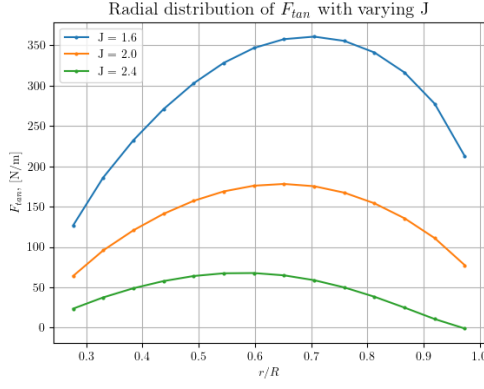
These induced velocities alter the effective  $\alpha$  and influence both lift and drag distribution across the blade— oversimplified by BEM due to independence of blade segments. As a result, LLM provides a more physically consistent and accurate  $\Gamma$  distribution.

### 4.2.4 Radial Distribution of the Tangential Load

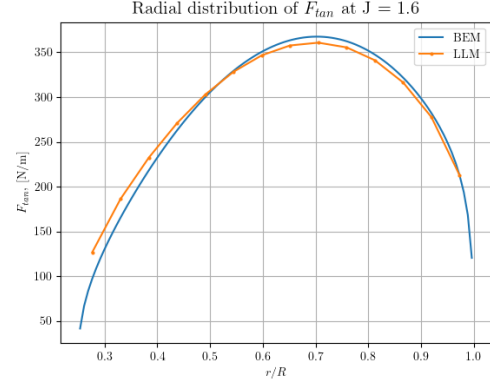
From Figure 6a, it is observed that  $F_{\tan}$  decreases with increasing advance ratio. This trend aligns with physical expectation; at higher  $J$ , the axial velocity dominates the tangential velocity, reducing the component of aerodynamic force in the tangential direction, and hence lowering torque.

$$F_{\tan} = \frac{1}{2} \rho V^2 c (C_L \sin \phi + C_D \cos \phi)$$

Here,  $c$  is the local chord length,  $V$  is the relative velocity at the blade element.



(a) Tangential Loads at varying  $J$ , in N/m

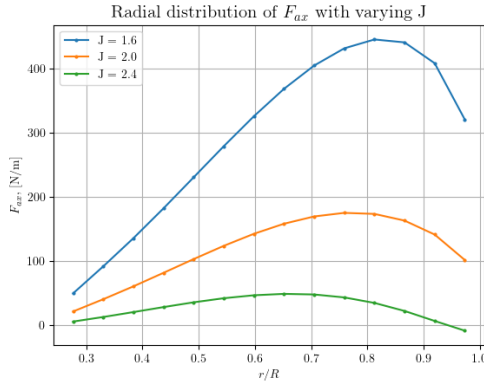


(b) Tangential load distribution from LLM and BEM

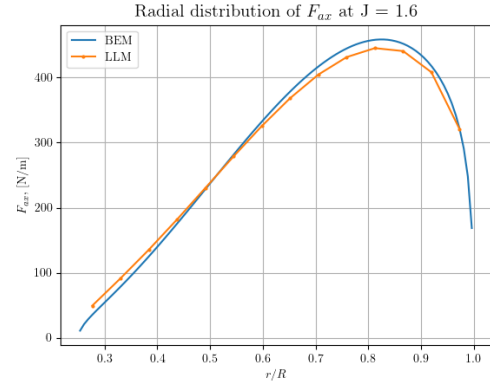
Figure 6: Radial distribution of tangential load.

In Figure 6b, the comparison between BEM and LLM at  $J = 1.6$  shows a high degree of consistency. Minor deviations appear near blade ends, where LLM accounts for wake interactions and induced effects due to its vortex-based formulation. The agreement confirms that both models predict torque distribution accurately.

#### 4.2.5 Radial Distribution of the Axial Load



(a) Axial Loads at varying  $J$ , in N/m



(b) Axial load distribution from LLM and BEM

Figure 7: Radial distribution of axial load.

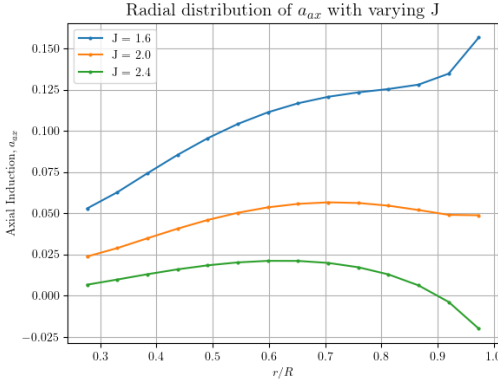
From Figure 7a, it is observed that axial load increases significantly as advance ratio decreases. At lower  $J$ , the inflow angle is reduced, resulting in a higher effective angle of attack and thus greater lift. This is realised as a higher axial force contribution across the blade. Conversely, at higher advance ratios like  $J = 2.4$ , the axial load decreases across the span due to lower aerodynamic loading. The formulation given by Equation 9 captures both lift-aligned and drag-induced components of the force acting in the axial direction.

$$F_{ax} = \frac{1}{2} \rho V^2 c (C_L \cos \phi - C_D \sin \phi) \quad (9)$$

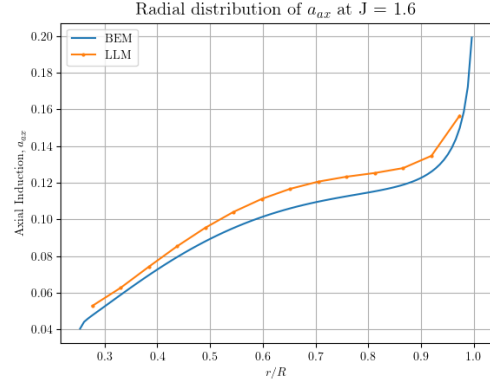
In Figure 7b, the comparison between BEM and LLM shows strong agreement throughout most of the span, with slight divergence near the mid-span. Although miniscule, the deviation from BEM results can be attributed to the circulation computed by LLM. As  $F_{ax}$  is dependent on many parameters which show slight variation between LLM and BEM, these errors creep into the calculation of  $F_{ax}$  as well. Hence slight deviation is noticeable, otherwise  $F_{ax}$  correlates to a good extent.

## 4.2.6 Radial Distribution of the Induction Factor

### Axial Induction Factor



(a) Axial induction at varying  $J$



(b) Axial induction from LLM and BEM

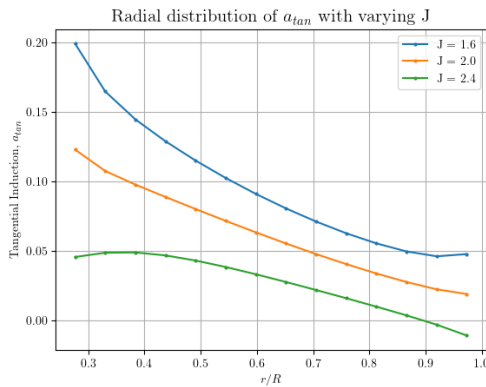
Figure 8: Radial distribution of axial induction,  $a$ .

From Figure 8a, it is evident that the axial induction factor decreases with increasing advance ratio. Low  $J$  correspond to higher axial loads which greatly affect the axial induction. At higher  $J$ , the rotor has a lower thrust coefficient, leading to lower induced deceleration and thus smaller values of  $a_{ax}$ . Axial induction is given by

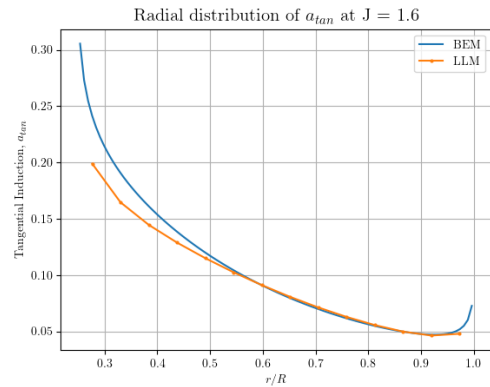
$$V_{axial} = V_{\infty}(1 + a)$$

In Figure 8b, the BEM and LLM predictions of  $a_{ax}$  are compared at  $J = 1.6$ . The trends agree well across most of the span, with slight deviations near the mid-span. It can be observed that the root and tip show somewhat similar trends. Since the lifting line model explicitly models the trailing vortices, this also implies that the Prandtl root and tip loss corrections made in the blade element momentum model is accurate enough at predicting vortex shedding at the tip.

### Tangential Induction Factor



(a) Tangential induction at varying  $J$



(b) Tangential induction from LLM and BEM

Figure 9: Radial distribution of tangential induction,  $a$ .

The tangential induction factor decreases with increasing advance ratio as seen in Figure 9a. At higher  $J$ , the rotational speed of the rotor has a less dominant effect, which decreases the tangential induction factor. The tangential induction factor modifies the local tangential velocity as:

$$V_{tan} = \Omega r(1 - a')$$

In Figure 9b, the comparison of BEM and LLM predictions at  $J = 1.6$  shows good agreement across much of the span, with slight differences in the root region. This is due to the purely analytical nature of the Prandtl root and tip corrections used in BEM.

In summary, both axial and tangential induction factors show expected trends with increasing advance ratio:  $a$  and  $a'$  decreases. Further, there was satisfactory correlation between the LLM and BEM models.

#### 4.2.7 Thrust ( $C_T$ ) and Power Coefficient ( $C_P$ )

Table 1: Comparison of BEM and LLM results at different advance ratios

Advance Ratio ( $J$ )	CT		CP	
	BEM	LLM	BEM	LLM
1.6	0.3339	0.3333	0.5342	0.5332
2.0	0.2064	0.2093	0.4129	0.4186
2.4	0.0675	0.0699	0.1620	0.1678

Table 1 summarizes the total thrust and power coefficients predicted by BEM and LLM at different advance ratios. Both  $C_T$  and  $C_P$  decrease with increasing  $J$ . This is because, as the advance ratio increase, the angle of attack decreases. Hence, the lift generated by the propeller blade decreases, consequently the thrust decreases.

At all the advanced ratios, the difference between BEM and LLM is of the order  $\mathcal{O}(10^{-3})$ , and both models produce nearly identical results. This indicates that both methods are equally effective at accurately predicting the thrust and power coefficient.

### 4.3 Sensitivity Analysis

The robustness of the lifting line model is investigated by examining its sensitivity to various modeling parameters. While there could be many independent parameters, four are chosen— initial guess for convection velocity, blade discretisation scheme, number of wake vortex filaments, and the total wake length. These analyses help identify convergence behavior, and sensitivity to the LLM model to input parameters.

#### 4.3.1 Assumed Convection Speed for Frozen Wake

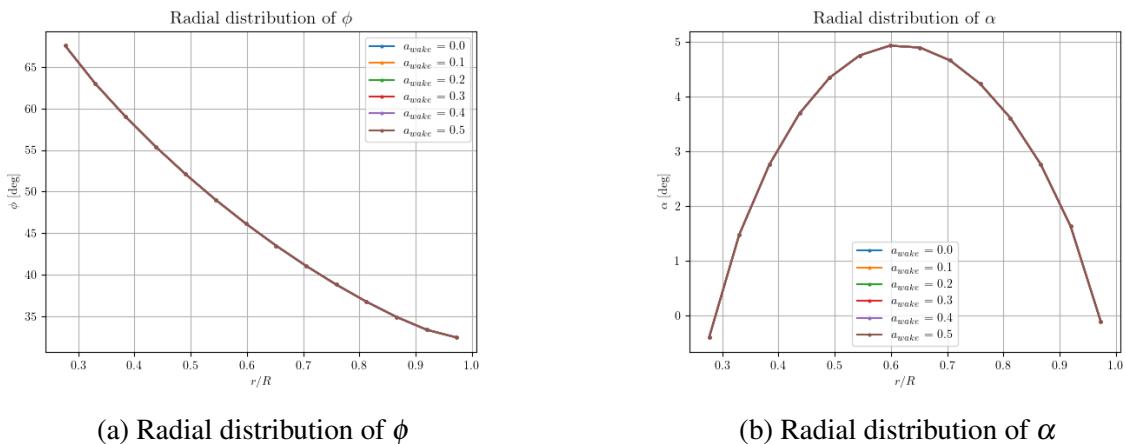
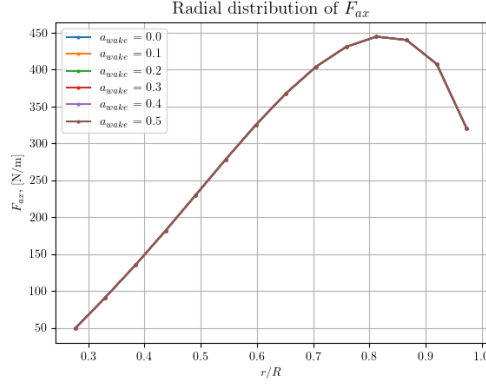
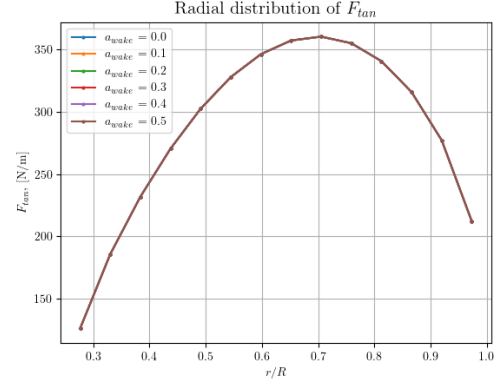


Figure 10: Sensitivity of  $\alpha$  and  $\phi$  to change in wake velocity.



(a) Radial distribution of axial load



(b) Radial distribution of tangential load

Figure 11: Sensitivity comparison of axial and tangential load for assumed convection speed.

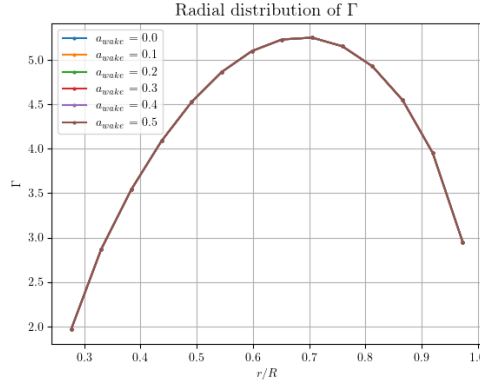


Figure 12: Sensitivity comparison of radial distribution of  $\Gamma$

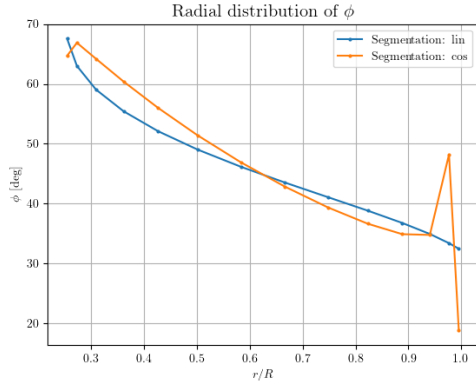
Figure 10, 11 and 12 show the sensitivity of the lifting line method to the initial guess for axial induction factor. All other parameters, including geometry, operating conditions, and discretization, were held constant. The wake convection speed ( $U_w$ ) was varied by varying the assumed wake induction factor ( $a_w$ ) values from 0.0 to 0.5 in steps of 0.1. The relation between the wake induction factor and wake convection speed is given by

$$U_w = V_\infty(1 + a_w) \quad (10)$$

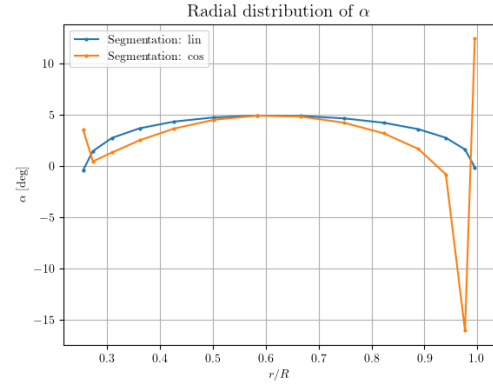
As shown in the figures, it can be observed that all the aerodynamic parameters have no visible variation as the assumed wake convection speed is varied. This occurs due to change in the wake induction factor after each iteration. Hence the geometry of the wake is updated after each iteration, and it is seen that the initial guess does not have an effect on the converged values of the aerodynamic parameters.

Hence, the LLM implementation is numerically stable and insensitive to the choice of initial induction guess, ensuring reliable convergence.

### 4.3.2 Type of blade segmentation

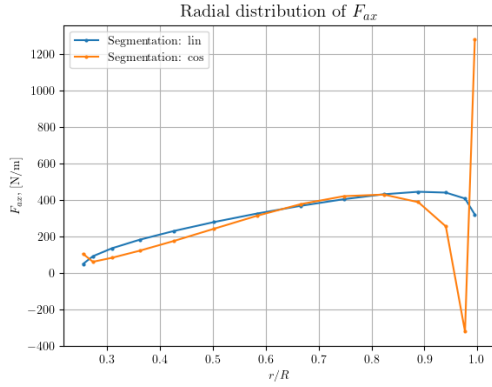


(a) Radial distribution of  $\phi$

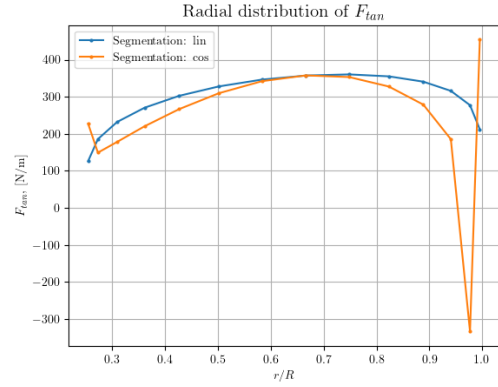


(b) Radial distribution of  $\alpha$

Figure 13: Sensitivity Results of discretisation of blade on  $\alpha$  and  $\phi$



(a) Radial distribution of axial load



(b) Radial distribution of tangential load

Figure 14: Sensitivity comparison of axial and tangential loads for discretisation of blade

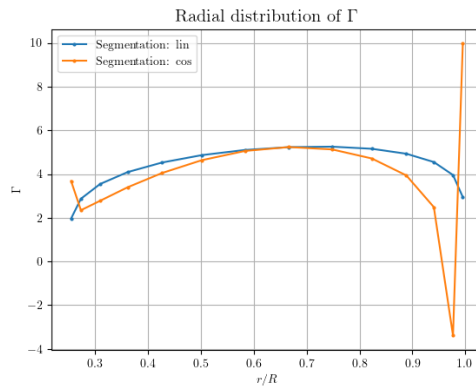


Figure 15: Sensitivity results comparison of  $\Gamma$  for discretisation of blade

The above figures presents the sensitivity of the lifting line model to blade discretization strategy, comparing linear spacing (blue) and cosine spacing (orange) of control points along the span. Both approaches use the same number of segments, differing only in how points are distributed.

As seen in Figure 13a and Figure 13b, the inflow angle ( $\phi$ ) and the angle of attack ( $\alpha$ ) both show a prominent spike near the tip and a noticeable divergence near the root for cosine spacing. This spike arises due to denser clustering of control points in those regions, which amplifies sensitivity to induced velocities in that region. Higher degree of discretisation leads to potential numerical instabilities which hinder the result obtained.

From Figure 14, similar trends can be observed in axial load near the tip and the root for cosine spacing. the mid-span trend is mostly similar. Similar line of reasoning as employed above accurately explains this anomaly. Tangential load in Figure 14b shows a similar trend in the curves, with the root and tip for the cosine spacing having a spike.

The circulation profiles in Figure 15 confirm this: cosine spacing produces a sharp, unrealistic spike in  $\Gamma$  near the tip and a smaller spike near the root, whereas linear spacing yields a smoother and more physically reasonable decay.

In conclusion, although cosine spacing is theoretically advantageous for resolving gradients, in this implementation it introduces numerical instabilities at the tip due to over-sensitivity in tightly clustered regions. Linear spacing, provides more stable and physically consistent results in this case. This highlights the importance of matching discretization strategy to the model's robustness and numerical treatment.

#### 4.3.3 Number of Vortex Filaments

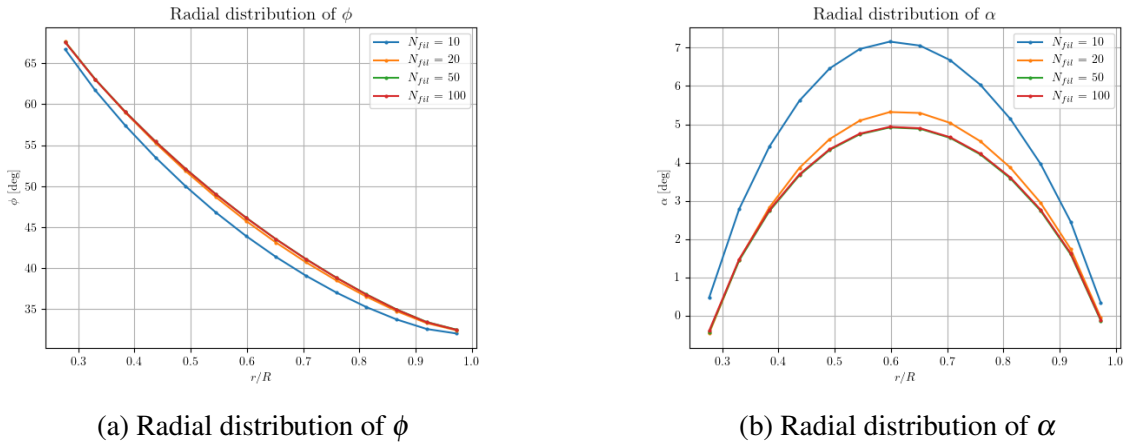
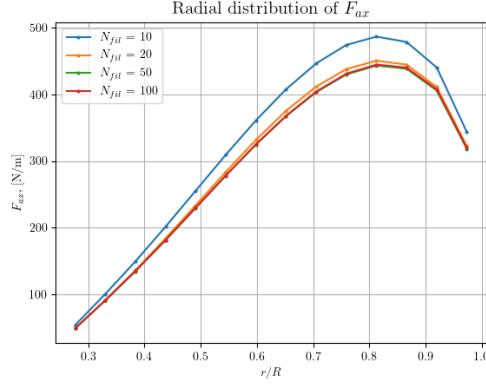
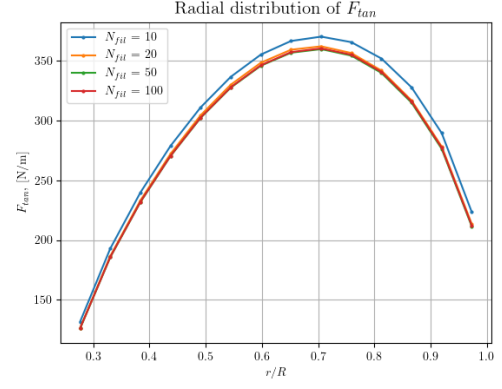


Figure 16: Sensitivity Results of no. of wake segments of  $\alpha$  and  $\phi$



(a) Radial distribution of axial load



(b) Radial distribution of tangential load

Figure 17: Sensitivity comparison of axial and tangential loads for number of wake segments

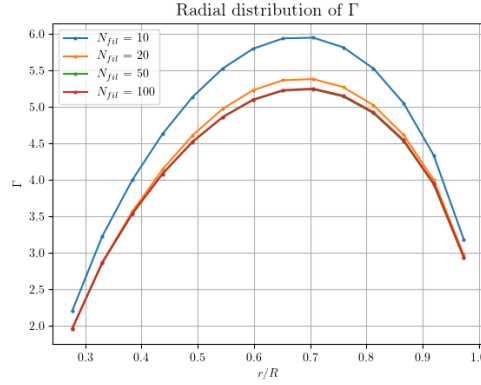


Figure 18: Sensitivity results comparison of  $\Gamma$  for number of wake segments

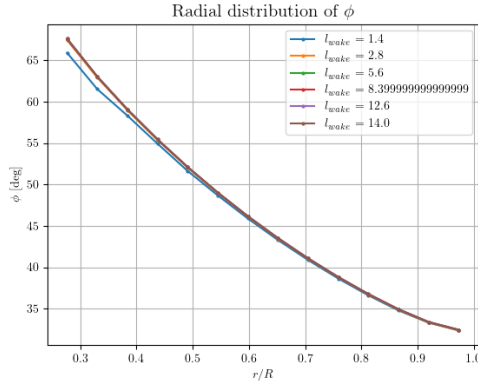
Figures above assess the influence of wake filament count on the accuracy of the lifting line method. Simulations were performed using 10, 20, 50, and 100 segments, with linear spacing applied in all cases.

From Figure 16, Figure 17, and Figure 18, it can be seen that the inflow angle, the angle of attack, axial and tangential loads, and circulation show the same variation. The results with 10 vortex filaments are significantly under-resolved. As the number of vortex filaments in the wake discretization increases, the trends of these parameters get closer to a statistically converged curve. From 20 segments onward, results become progressively smoother, with minimal improvement beyond 50 segments. This is according to expected trend since as the number of vortex filaments in the wake is increased, the wake is modeled more accurately.

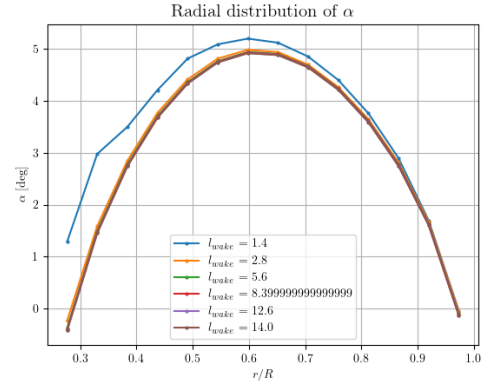
Overall, this study shows that 10 segments are insufficient and lead to inaccurate predictions. A minimum of 20 is needed for acceptable fidelity, while 50 segments offer near-converged results. Using more than 50 provides only marginal gains for steady-state analysis.



### 4.3.4 Wake Length

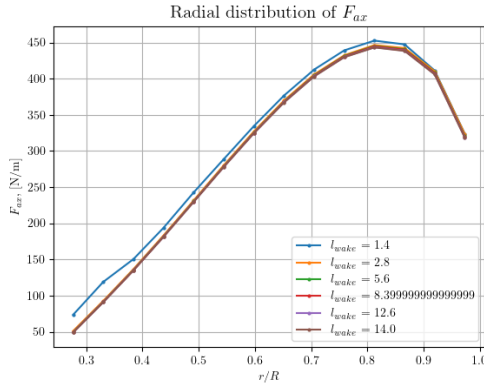


(a) Radial distribution of  $\phi$

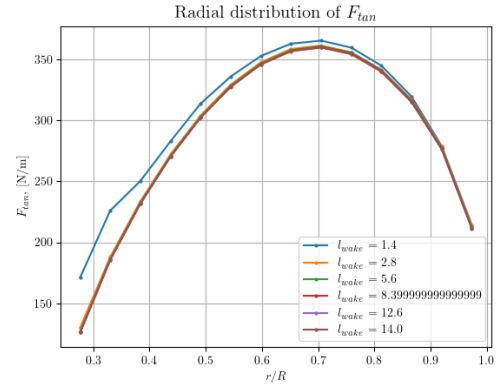


(b) Radial distribution of  $\alpha$

Figure 19: Sensitivity Results of wake length of  $\alpha$  and  $\phi$



(a) Radial distribution of axial load



(b) Radial distribution of tangential load

Figure 20: Sensitivity comparison of axial and tangential loads for wake length

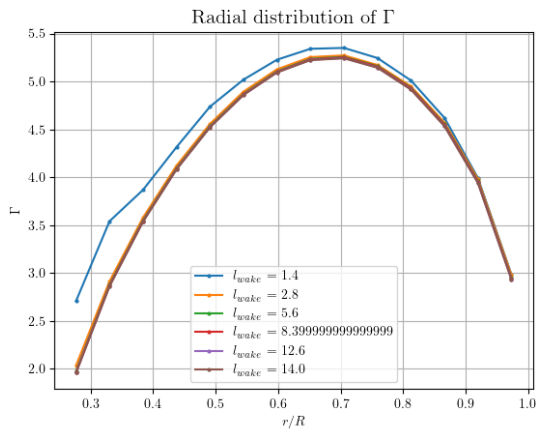


Figure 21: Sensitivity of  $\Gamma$  to wake length

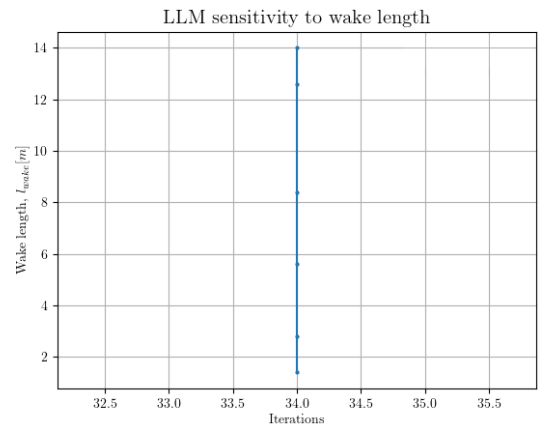


Figure 22: LLM sensitivity to wake length

It can be observed from [Figure 19](#), [Figure 20](#), and [Figure 21](#) that the inflow angle, angle of attack, axial and tangential load, and circulation show similar trends. For wake length,  $L_w = 1.4$  (or  $1 \times D$ ), there is

a noticeable difference in the curves. However, as  $L_w$  increases, the curves start to superimpose. This convergence can be seen after  $L_w \approx 4D$ . A wake length of 5 or more yields consistent and reliable results across the entire blade span.

Figure 22 shows that there is no change in the computational time or iteration number as the length of the wake increases. This indicates that the solver stability is unaffected by this parameter. This is according to expectations because the way the wake is discretized. It is discretized such that the total number of wake filaments are defined in the entire length of the wake. Hence, the number of vortex filaments in the wake remains the same regardless of the wake length and the convergence time is the same.

## 5 Conclusion

Through this study, both Lifting Line Model and Blade Element Method have shown agreeable concurrence in their results. A sensitivity study reveals that LLM harbors remarkable robustness towards change in input parameters. It should be noted, that while cosine spacing causes numerical issues near the blade root and tip, it is highly dependent on the defined number of blade segments since a larger number could lead to a cluster of segments near the blade ends leading to "over"-discretization of blade, so much so that numerical instabilities creep in. Since the sensitivity study did not consider the number of blade segments as an independent parameter, the effectiveness of cosine spacing cannot be ascertained. However, it is the inference of the authors that for lower blade segments, cosine spacing could yield better results since a majority of segments are populated near the tips.

The BEM method, while built on several simplifying assumptions, such as independent blade elements, steady and axisymmetric flow, and the use of empirical loss corrections, has shown strong agreement with the LLM across key performance metrics including inflow angle, angle of attack, circulation, and load distributions. Its primary strengths lie in simplicity and computational efficiency, making it highly suitable for rapid design iterations and preliminary performance estimations.

On the other hand, the Lifting Line Method offers a more physically grounded framework by explicitly modeling the wake using vortex filaments and computing induced velocities via the Biot–Savart law. This allows LLM to inherently account for spanwise aerodynamic coupling and wake influence, particularly improving accuracy near the blade root and tip—regions where BEM’s simplified corrections fall short. The sensitivity analysis performed revealed that while the LLM is robust against initial induction guesses and wake length assumptions, its predictions can be affected by discretization choices and insufficient wake resolution.

Despite its higher computational demand, the LLM provides a clearer representation of the flow physics and is more appropriate when detailed load distributions and interaction effects are of interest. However, for preliminary calculations, BEM remains a reliable and sufficiently accurate method. The comparative study confirms that both approaches, when implemented carefully, yield consistent overall trends, but LLM’s explicit treatment of induced effects offers superior fidelity for high-resolution aerodynamic analysis.

## 6 References

1. Delft University of Technology, "Rotor/Wake Aerodynamics Assignment 1 2024–25", Faculty of Aerospace Engineering, 2024.
2. G. van Kuik, The Fluid Dynamic Basis for Actuator Disc and Rotor Theories. 2018. [Online]. Available: <https://doi.org/10.3233/978-1-61499-866-2-i>
3. M. K. Rwigema, "Propeller blade element momentum theory with vortex deflection," in Proc. ICAS, ICAS 2010-2.3.3, Nice, France, 2010.
4. "Blade Element Propeller Theory," Aerodynamics for Students. [Online]. Available: <https://www.aerodynamics4students.com/propulsion/blade-element-propeller-theory.php>
5. E. Branlard, Wind Turbine Aerodynamics and Vorticity-Based Methods: Fundamentals and Recent Applications. Cham, Switzerland: Springer, 2017.